Journal of Solid State Chemistry **145,** 503–510 (1999)
Article ID jssc.1999.8195, available online at http://www.idealibrary.com on IDEAL®

First Principles Calculation of Electrode Material for Lithium Intercalation Batteries: TiS_2 and $LiTi_2S_4$ Cubic Spinel Structures

Ľubomír Benco,[1] Jean-Luc Barras, Michail Atanasov,[2] Claude Daul

Institute of Inorganic Chemistry, University of Fribourg, Pérolles, CH-1700 Fribourg, Switzerland
E-mail: benco@savba.sk

and

Eric Deiss

Paul Sherrer Institute, CH-5232 Villigen PSI, Switzerland

Received September 14, 1998; in revised form February 2, 1999; accepted February 3, 1999

DEDICATED TO PROFESSOR PETER DAY ON HIS 60TH BIRTHDAY

The cubic spinel structures, TiS_2 and $LiTI_2S_4$, have been fully optimized using the full-potential linearized augmented-plane-wave (LAPW) method. The comparison between band structures of TiS_2 and $LiTi_2S_4$ and the analogous oxide structures indicates that bonding in sulfides is more covalent. Bonding of both sulfides and oxides becomes more ionic after Li intercalation. The calculated average intercalation voltage of 2.16 eV ($LiTi_2S_4$) and 2.93 eV ($LiTi_2O_4$) is in good agreement with experimental data. The higher voltage of oxide is due to the larger change of enthalpy of formation between reactants and products. © 1999 Academic Press

INTRODUCTION

In the last decade there has been considerable activity in research and development of rechargeable lithium-ion batteries (1, 2), also referred to as rocking chair, shuttlecock, or intercalation batteries. Their high energy density makes them suitable for electronic devices as well as for electric vehicles. The (negative) anodes and (positive) cathodes consist of materials which can intercalate lithium ions. During discharge lithium moves from the anode through an electrolyte into the cathode. Carbons (3, 4) and metal oxides (5) are mainly used as anodic and cathodic materials, respectively. The first commercial battery of this type was developed by Sony (6–8), who used coke and cobalt oxide as electrode materials. This battery was reported to be operative over more than 1200 cycles with an average voltage of 3.6 V. Similar cycle numbers and average voltages could be achieved with the systems coke/nickel oxide (9) and coke/manganese oxide (10). Low cost and environmental reasons focused the development on spinel type manganese oxides as cathodic material, and commercial batteries of this type have been availablle by Nippon Moli Energy since 1996. Electrode materials such as titanium oxide (11) or titanium sulfide (12) can be used either as cathodic or anodic materials. Such systems have a lower voltage and therefore a lower energy density than the systems mentioned above, but their higher stability makes them competitive too, and in 1995 the Japanese company Matsushita brought a battery onto the market consisting of a spinel type titanium oxide anode and a spinel type manganese oxide cathode.

A great amount of experimental data in this area is now available. Collecting these data and analyzing them with appropriate computational models is a way to obtain better insight into the physical and chemical processes. These models can be used to reduce the experimental effort and to design improved batteries.

First principles calculations are a modeling tool which requires only the crystal structure as input. Such calculations are therefore free of unknown parameters. In the last few years this tool has became more and more popular in the design of lithium-ion batteries and has been used by many authors (13–23).

[1] To whom correspondence should be addressed. Permanent address: Institute of Inorganic Chemistry, Slovak Academy of Sciences, Dúbravská cesta 9, SK-84236 Bratislava, Slovak Republic; telephone, +421 7 59410468; fax, +421 7 59410444.

[2] Permanent address: Institute of Inorganic Chemistry, Bulgarian Academy of Sciences, B1.11, 1113 Sofia, Bulgaria.

0022-4596/99 $30.00

TiS_2 is an electrode material of interest in Li-based cells (24, 25). The Li intercalation into TiS_2 was characterized in layered trigonal CdI_2-type crystal structure, for which Umrigar *et al.* (26) presented LAPW calculations of the band structure and effect of interlayer interactions on the electronic structure. In this paper we extend the study of Umrigar *et al.* with the first principles structure optimization of both the Li-extracted and Li-intercalated compound. From the three structure modifications of TiS_2 (trigonal (27), monoclinic (28), and cubic (29)) for the purpose of the structure optimization we have chosen the simplest cubic structure. Upon Li intercalation into cubic TiS_2 the spinel structure is not obtained. Li occupies the tetrahedral 8*a* sites, but also octahedral 16*c* sites, and the intercalation in fact always ends with the trigonal structure ($P\bar{3}m1$) (30–33). Our recent results, however, show that the voltage of a solid material does not depend on the structure but on the oxidation state of the transition metal (20). In this paper, therefore, for the sake of simplicity, we keep the Li-intercalated structure cubic, thus modeling the topotactic intercalation. For optimized structures we characterize the changes of geometries, electronic structures, and electron densities and compare them with corresponding changes in structures of cubic oxides. In the last paragraph we calculate enthalpies of formation (EOF) of reactants and products and compare calculated average intercalation voltages (AIV) with experimental measurements.

METHOD AND COMPUTATIONAL DETAILS

The first-principles all-electron full-potential LAPW method (34) as implemented in the WIEN97 code (35) is used to perform electronic structure calculations. Core states are treated fully relativistically (36) and for valence states relativistic effects are included in a scalar relativistic treatment (37). The exchange and correlation potential is parametrized within the generalized-gradient approximation (GGA) according to Perdew and Wang (38). The maximum l value in the expansion of the basis set inside atomic spheres is 8 and 4 for the computation of muffin-tin and non-muffin-tin matrix elements, respectively. A grid of 781 points is chosen for the evaluation of functions inside atomic spheres. The parameter $R_{mt}K_{max} = 8$ (where R_{mt} is the smallest atomic sphere radius in the unit cell and K_{max} is the magnitude of the largest K vector) leads to an energy cutoff of $E_{cut} \approx 360$ eV for the expansion of plane waves in the interstitial regionl. Performing the structure optimization we have used a set of 4 k oints. Electronic properties for the optimal structures are evaluated using a set of 35 k points in the ireducible wedge of the face-centered cubic Brillouin zone (BZ). The self-consistency is typically reached in 10 iterations, when the total energy is stable to within 0.1 mRy between successive iterations.

STRUCTURE OPTIMIZATION

In the cubic spinel structure of TiS_2 the close-packed array of S atoms is located at the 32*e* positions of the space group $Fd\bar{3}m$ and the Ti atoms occupy half of the octahedral sites (designated as 16*d*). In the lithium-intercalated structure of $LiTi_2S_4$ lithium atoms occupy the eight tetrahedral sites designated as 8*a*. There are two variable parameters in the spinel structure: the lattice parameter a and an internal parameter x. The structures of both compounds TiS_2 and $LiTi_2S_4$ were fully optimized with respect to these two variable parameters. The optimized parameters along with available experimental data are listed in Table 1 and coordination spheres of the Ti and Li atoms are visualized in Fig. 1.

For TiS_2 the calculated lattice parameter is $\sim 1\%$ larger than that obtained by X-ray diffraction from the powder (29). The TiS_6 octahedra are not ideal but slightly deformed (cf. S–Ti–S angles). The calculated deformation, however, is opposite in sign to that determined experimentally. In the planar arrangement of 2 Ti and 2 S atoms, the experimental structure shows slight shortening of the Ti–Ti distance, while the LAPW optimization predicts shorter S–S distances (cf. Ti–Ti and S–S distances, and S–Ti–S angles). It should be mentioned that optimized geometry parameters and the pattern of the deformation of another cubic spinel $LiTi_2O_4$ (21) are in very good agreement with the single crystal structure determination (39). There is, however, insufficient evidence to explain the difference between the experimentally determined structure (29) and our calculations.

The intercalation of Li into tetrahedral voids causes an expansion of the unit cell with the increase of the lattice parameter by 2.7%. As a result of the expansion all interatomic distances are increased except that of the S-to-S second neighbors. This means that Li intercalation causes the increase of the structure deformation, measured as a deviation of the geometry parameters from values of ideal octahedra, which are 90° for the S–Ti–S angle and 0.25 for the internal parameter x.

TABLE 1
Geometry Information on Spinel $LiTi_2S_4$ and Corresponding Li Deintercalated TiS_2 Structures[a]

	Space group	a (Å)	z (–)	V (Å^3)	Ti–S (Å)	Ti–Ti (Å)	S–S (Å)	S–Ti–S (degrees)
TiS_2	$Fd\bar{3}m$	9.85	0.2524	955.7	2.44	3.48	3.42	88.9
		(9.739)	(0.2488)	(923.7)	(2.45)	(3.44)	(3.48)	90.5
$LiTi_2S_4$	$Fd\bar{3}m$	10.12	0.2578	1036.4	2.45	3.58	3.35	86.3

[a]Available experimental data are given in parentheses (29).

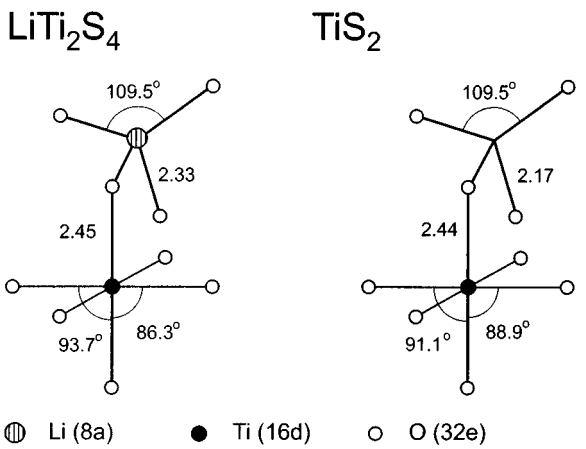

FIG. 1. The geometry parameters of the coordination sphere of Ti and Li atoms of optimized structures of TiS_2 and $LiTi_2S_4$.

ELECTRONIC STRUCTURE

Density of State

The total and the partial DOS evaluated for optimized structures are shown in Fig. 2. The scale of all spectra is situated relative to the valence-band maximum (second band from the left). The distribution of energy states in both, Li-extracted (Fig. 2a) and Li-intercalated (Fi. 2b) systems, is similar. Energy states of the valence region are collected in three main bands. They are (from left) *s*, *p*, and *d* bands. The last band is split due to the cubic symmetry into "t_{2g}" and "e_g" components. The classification of bands is given at the top of Fig. 2a. The partial DOS show that main orbital components of the bonding come from S (3*s*) in the *s* band, S (3*p*) in the *p* band, and Ti (3*d*) in the *d* band. In TiS_2 the Fermi level (E_F) is situated in a dip between the fully occupied *p* band and the unoccupied *d* band. Note the slight overlap of these two bands, which means that cubic TiS_2 is a semimetal. In contrast to trigonal layered TiS_2 which is a semimetal with an indirect *p–d* overlap (26), the overlap in cubic spinel TiS_2 is direct at the Γ point. In $LiTi_2S_4$ the extra electron supplied with the intercalated Li atom occupies the lowest states of the "t_{2g}" band, the E_F is therefore shifted up into the *d* band and Li-intercalated compound becomes conducting. On the filling of the *d* band the *p–d* overlap vanishes due to the bonding/antibonding repulsion and an energy gap of 0.365 eV appears.

Interaction Scheme

Figure 3 shows interaction schemes for TiS_2 and $LiTi_2S_4$ constructed as solid state analogues of molecular orbital schemes according to the recently proposed procedure (40–42). In such a scheme the total DOS is displayed together with free-atom energy levels on the real energy scale. To this propose the total DOS is shifted to the position comparable with atomic energy levels. The schemes, displayed in Fig. 3, are constructed from calculated total DOS (cf. Fig. 2) complemented with free-atom eigenvalues. The total DOS in the scheme of TiS_2 (Fig. 3, left) is shifted to fix the topmost occupied part of the *p* band, which corresponds to S (3*p*) nonbonding states, to the S (3*p*) free-atom eigenvalue. In the scheme these highest occupied nonbonding states are indicated with filled area. With the total DOS in this position the scheme provides fully consistent and not controversal picture of the bonding, *i.e.*, the *s* band is slightly stabilized compared to the atomic S (3*s*) level, the *p* band

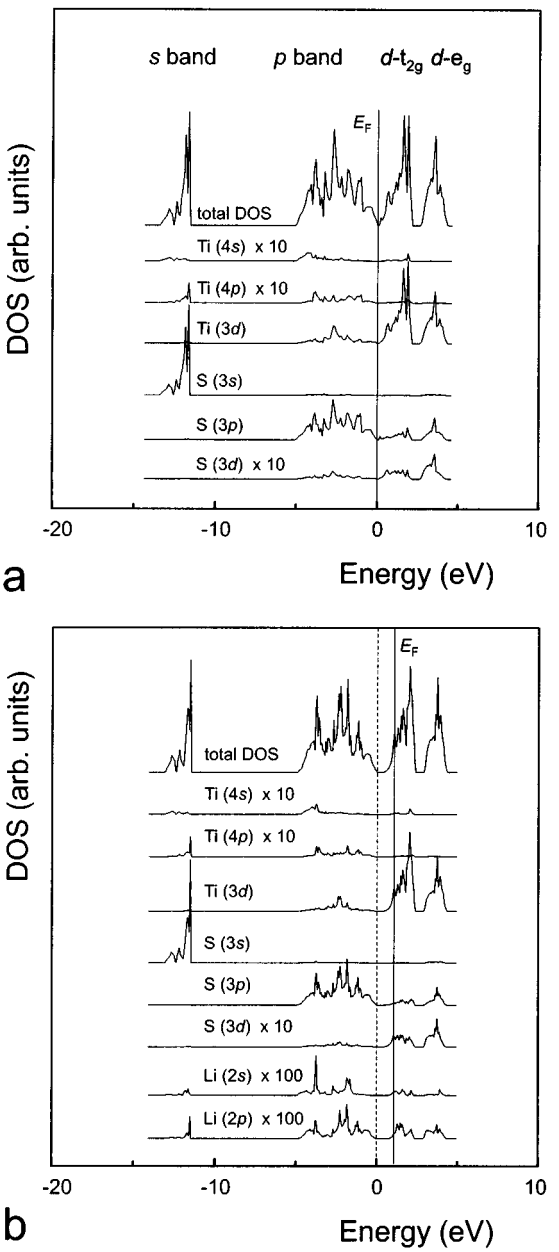

FIG. 2. The total and partial density of states of TiS_2 and $LiTi_2S_4$.

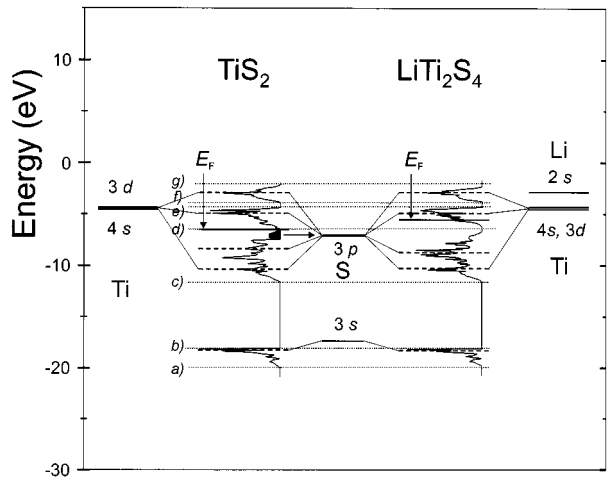

FIG. 3. The interaction scheme of TiS_2 and $LiTi_2S_4$.

is clearly derived from the S (3*p*) level, and the position of two *d* bands shows that the t_{2g} band is rather nonbonding and the e_g component is clearly Ti–S antibonding. The position of the total DOS of $LiTi_2S_4$ (Fig. 3, right) is adjusted according to band edges of the DOS in TiS_2. These are indicated with dotted horizontal lines. Figure 3 shows that, in spite of the Li atoms present within the structure, the dispersion of energy states is very similar to that of the Li-extracted compound. In the DOS of $LiTi_2S_4$ the most edges (*b*, *c*, *e*, and *f*) are retained. Slight deviations which are due to the intercalation of Li are discussed later.

An effective bonding is driven by two factors: the overlap between atomic orbitals and the energy matching of interacting levels (ΔE_{ab} for orbitals *a* and *b*). Both these features, orbital interactions and energy matching are displayed in simple terms in Fig. 3. The interaction scheme thus provides compact representation of chemical bonding showing characteristic features such as orbital interactions, bonding properties of states, and covalency/ionicity relations.

The pattern of bonding in TiS_2 and $LiTi2S_4$ is 1 : 1 because there is only one major orbital interaction: S (3*p*)-to-Ti (3*d*). A large overlap of these orbitals, and rather good energy matching ($\Delta E_{S3p\text{–}Ti3d} \cong 2.75$ eV) indicates considerable covalency of bonding, what makes this orbital interaction dominant and responsible for the large width of the *p* band. Another feature proving the covalency of the S (3*p*)-to-Ti (3*d*) orbital interaction is admixture of Ti (3*d*) states to the *p* band. Note in Fig. 2a that this admixture raises a proportional amount of S (3*p*) states into the *d* band. This bonding/antibonding splitting of atomic S (3*p*) and Ti (3*d*) states, which is due to the covalent orbital interaction, is in the interaction scheme (Fig. 3) indicated with interaction lines (40–42). These show that some part of states is stabilized, shifted down, and some part destabilized. Note in Fig. 3 that only S (3*p*) and Ti (3*d*) are split in this way. The S (3*s*) states are only slightly stabilized and form a narrow band at the bottom of the spectrum. There is some overlap between S (3*s*) and Ti (3*d*) orbitals allowed by symmetry. The large energy difference between two levels ($\Delta E_{S3s\text{–}Ti3d} \cong$ 13.01 eV), however, prevents effective covalent S (3*s*)-to-Ti (3*d*) bonding. The *s* band thus remain of atomic S 3*s* character. Its states are rather nonbonding with only small covalent admixture of Ti 3*d* states. This covalency, however, causes a broadening of the band toward more negative energies. The lower part of the band therefore consists of more covalent states and the sharp peak at the upper adge of the band is typical for nonbonding ionic states.

The states of the *d* band contain admixture of S 3*p* antibonding states. Figure 2a shows that there is a much larger admixture within the e_g subband. This could be therefore characterized as a band of Ti 3*d*-to-S 3*p* antibonding states. Because the major part of the t_{2g} subband resides at approximately the same position as the Ti 3*d* free-atom energy levels, these states are Ti-to-S nonbonding. The stabilizing broadening of the band comes from symmetry allowed t_{2g}–t_{2g} metal-to-metal interactions.

The interaction scheme of $LiTi_2S_4$ shows that upon intercalation of Li main features of bonding are retained. The position of the DOS shown in Fig. 3, right, keeps edges indicated with lines *b*, *c*, *e*, and *f* in same positions as in TiS_2. All bands, however, show slight narrowing. While in the *s* band the lower covalent part of the band is narrowed, the upper of the *p* band is shifted down in energy, thus opening the energy gap between the *p* and the *d* states. The values of bandwidth are listed in Table 2. The width of a band due to the interaction between two atoms strongly depends on the interatomic distance. Both, the bandwidth and the interatomic distance, however, have similar relation to the covalency/ionicity of bonding. Covalent bonds with increased electron density inbetween atoms are typically shorter and corresponding energy bands are broader (43). From this point of view the *s* bands in TiS_2 and $LiTi_2S_4$ are almost three times more ionic than the *p* bands. The intercalation of Li causes narrowing of both *s* and *p* band by the values of 0.18 and 0.16 eV, respectively. This means that the intercalation of Li atoms makes bonding within the spinel structure of TiS_2 more ionic. A similar effect was found for Li intercalation into cubic spinel structure of TiO_2 (21). The

TABLE 2
Widths of *s* and *p* Bands of $LiTi_2S_4$ and $LiTi_2O_4$ and Corresponding Li Deintercalated Cubic Spinel Structures (eV)

	TiS_2	$LiTi_2S_4$	$\Delta(TiS_2\text{–}LiTi_2S_4)$	TiO_2	$LiTi_2O_4$	$\Delta(TiO_2\text{–}LiTi_2O_4)$
s band	1.78	1.60	0.18	1.73	1.51	0.22
p band	5.10	4.94	0.16	4.74	4.61	0.13

bandwidth of cubic TiO_2 and $LiTi_2O_4$ are in Table 2 given for reference.

It is often considered that the close-packed anions are close enough for their *p* orbital to overlap and the anion-to-anion interaction could be one of important factors driving structural modifications of inorganic compounds. In our interaction schemes only interactions of nearest neighbors are analyzed. The total DOS, however, comprises all possible interactions. The fact that main features of bonding are easily derived from interactions of nearest neighbors indicates that second-neighbor interactions are of much less importance. This is due to much smaller orbital overlap in the second-neighbor arrangement. The larger dimensions of the *d* orbitals, however, cause that in TM compounds the effective second-neighbor t_{2g}–t_{2g} bonding occurs. Analyses of the metal-to-metal bonding have shown that states which are due to such an interaction appear as a low-energy shoulder of the t_{2g} band (44). Such states are apparent in the total DOS of both TiS_2 and $LiTi_2S_4$ (cf. Figs. 2 and 3). While in TiS_2 they are the empty intercalation of Li, provides an extra electron which fills a fraction of these slightly bonding states. Because the filling increases the enthalpy of formation the interaction of Li is a spontaneous process. Note that without effective *d*–*d* interaction all the states of the t_{2g} band in TiS_2 would be nonbonding and no Li intercalation would be possible. Contrary to the existence of bonding states which are due to the t_{2g}–t_{2g} second-neighbor contacts there is no evidence for the anion *p*–*p* interactions. If effective such an interaction would cause broadening of both *s* and *p* "anion" bands. Figures 2 and 3 and Table 2 show that in the situation when the bands are narrowed due to the more ionic metal–anion bonding effects of anion–anion broadening would be apparent in the total DOS. Our DOS calculated for optimized structures of TiS_2 and $LiTi_2S_4$ provide the evidence that the anion–anion bonding is negligible.

The t_{2g}–e_g splitting is slightly diminished upon Li intercalation (Fig. 3, right). While in TiS_2 the maximum splitting, measured from the bottom of the t_{2g} band to the top of the e_g band, is 4.29 eV, in $LiTi_2S_4$ this value is 3.95 eV. The magnitude of this ligand field splitting depends on the Ti–S distance. The increase in Ti–S distances which occurs with the increased ionicity therefore causes the decrease of the ligand field splitting. Note that the position and the value of the energy gap between t_{2g} and e_g sub-bands is basically retained.

In $LiTi_2S_4$, the Li atoms are tetrahedrally coordinated with S atoms. Such an arrangement allows considerable overlap and could end with effective orbital interaction between Li (2*s*) and S (3*p*) orbitals. Because of poor energy matching of the two levels ($\Delta E_{Li2s\text{-}S3p} \cong 4.19$ eV) this interaction is very ionic and produces practically no new states within occupied valence bands. This means that Li atoms only supply the electron density which fills the lowest unoccupied states in the total DOS.

Figure 4 compares bonding of $LiTi_2S_4$ and $LiTi_2O_4$ (21). Note the small difference in the position of the total DOS in the two schemes. In $LiTi_2O_4$ the states of the *p* band are due to the larger electronegativity of O atoms, compared to S atoms, more stabilized and the upper edge of the *p* band is situated exactly at the position of the free-atom O (2*p*) level (21). In $LiTi_2S_4$ the total DOS is situated slightly higher, cf. the position of dotted horizontal line within the *p* band. The schemes show considerable differences of bonding in these two compounds. The much deeper position of the *s* band in the oxide is derived from deeper lying free-atom *s* level. This contributes to larger enthalpy of formation of $LiTi_2O_4$ (cf. next paragraph). The larger width of both the *s* and the *p* bands proves the larger covalency of bonding in $LiTi_2S_4$, which is in line with smaller electronegativity of the S atom.

In $LiTi_2S_4$ the t_{2g}–e_g splitting is considerably smaller compared to the oxide, as indicated with horizontal lines *b* and *d*. The maximum splitting of 4.59 eV in $LiTi_2O_4$ is diminished to 3.95 eV in $LiTi_2S_4$, as a consequence of the weakening of the ligand field. Note that the Ti-to-*nonmetal* distance of the value 2.02 Å is lengthened to the value of 2.45 Å in $LiTi_2S_4$. The energy gap between the t_{2g} and e_g components is lowered from 1.18 to 0.57 eV.

Electron Densities

Figure 5 shows the bonding effect in TiS_2 and $LiTi_2S_4$ displayed for the (110) plane. The difference electron density, constructed as a difference of the bonding valence density and the spherical atomic densities, is for both compounds displayed in Figs. 5a and 5b. In TiS_2 (Fig. 5a) bonding between Ti and S atoms causes the transfer of the electron density from Ti to S. The shape of the depleted region on Ti shows that the electron density is withdrawn from t_{2g} orbitals. The increase occurs on both, Ti and S atoms. Small

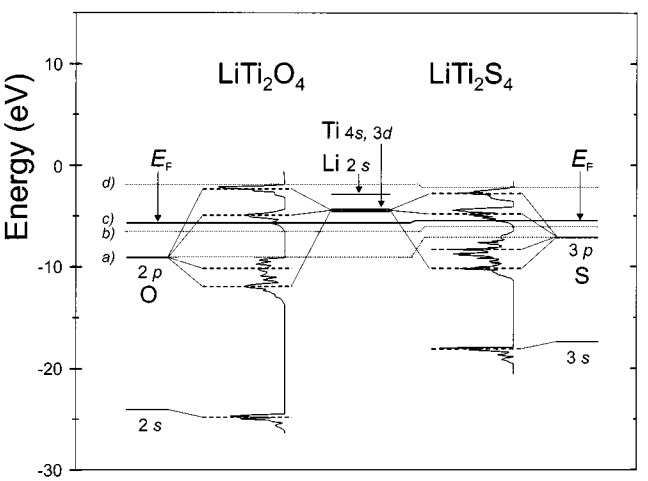

FIG. 4. The interaction scheme compared for $LiTi_2S_4$ and $LiTi_2O_4$.

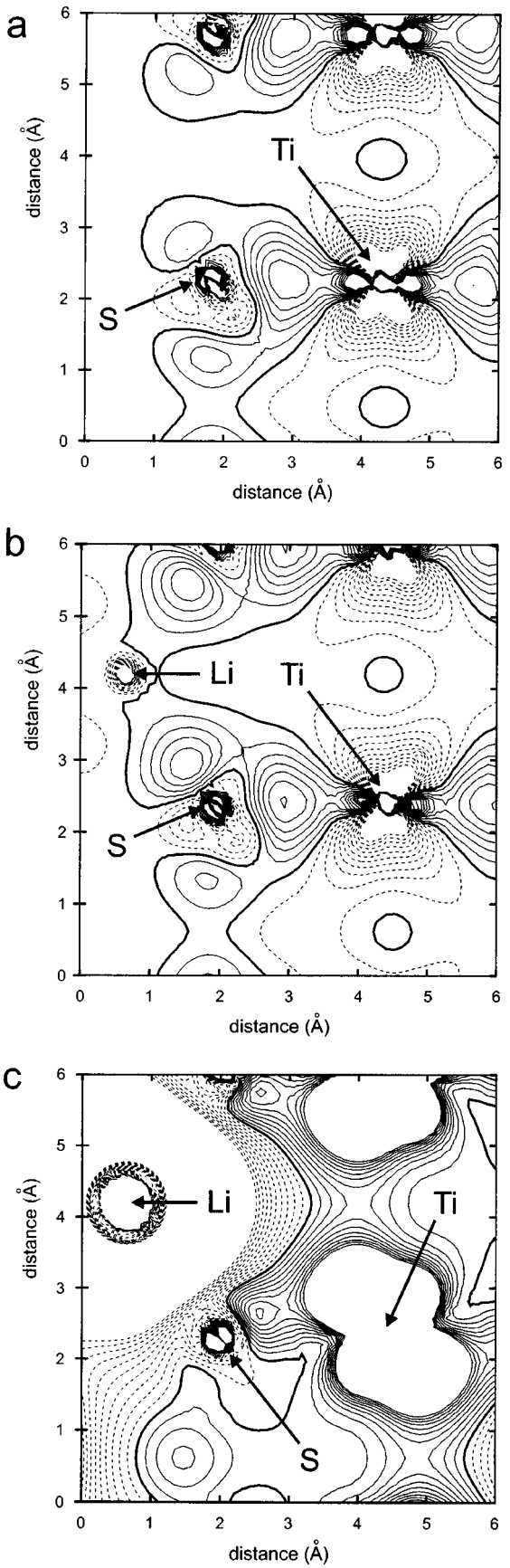

region of increased electron density on Ti is pointing toward the S atoms. This means that electrons are transferred into e_g orbitals which are mixed into the p band. The deformation of the electron density of the S atom is much more pronounced than that of the O atom (21), what proves that the electron cloud of S is much more "soft". Both the increase and the decrease of the electron density occurs on the S atoms in TiS_2. At the core and in the outer atomic region the electron density is increased. Note that while the core density is rather spherical, the increase in the outer atomic region of S atoms show remarkable directional properties. The largest increase is within the S–Ti bond. Note that one lobe of the increased electron density points also to the tetrahedral void into which Li atoms are intercalated.

The difference valence electron density in the Li intercalated compound is shown in Fig. 5b. It shows that intercalated Li atoms are strongly depleted of electron density. The spherical shape of the Li region proves the ionic character of the Li atoms. A comparison of Figs. 5a and 5b shows that a modification of bonding occurs upon the intercalation. The increase of the charge density on S atoms pointing toward Li is enlarged. The two maxima within the S–Ti bond are retained. One of them near the Ti atom, however, is diminished, and another one near the S atom is magnified. At the same time the height of the saddle point between the two maxima is lowered. All of these features confirm the increase of the ionicity of the S–Ti bond in $LiTi_2S_4$ which was already documented above with decreased bandwidth (Table 2) and increased bond length (Table 1).

Figure 5c shows the difference electron band-density (DEBD) constructed for a fraction of the electron density corresponding to one valence electron supplied to $LiTi_2S_4$ by Li atom upon the intercalation. In the DOS representation (Figs. 2b and 3, right) this density corresponds to occupied states at the bottom of the t_{2g} sub-band. The DEBD shows the transfer of the Li electron density to the covalent Ti–S skeleton of the compound. Figure 5c shows that the whole tetrahedral Li-centered void is strongly depleted of the electron density. The spherical pattern of the depletion confirms the ionic character of the electron cloud surrounding the Li atom. Its density is transferred mainly to the Ti atoms, where it fills the t_{2g} orbitals. As follows from Fig. 5c there is an increase of electron density of two kinds: Ti(t_{2g})-to-S(p) and Ti(t_{2g})-to-Ti(t_{2g}). In both of these orbital interactions, the increase of the electron density is not symmetric

FIG. 5. The difference electron densities within the (110) plane. (a) The difference density map of TiS_2. (b) The difference density map of $LiTi_2S_4$. (c) The difference band-density constructed for Li electron density in $LiTi_2S_4$. Continuous, thick continuous, and dashed lines indicate positive, zero, and negative values, respectively. Contour spacings are 0.02 e/Å^3 (a and b) and 0.001 e/Å^3 (c).

with respect to the lines connecting atomic nuclei. These two kinds of increased electron density were characterized also in cubic spinel oxides (21). Surprising is the fact that, in spite of the large increase of the lattice parameter and interatomic distances, these two kinds of weak bonding could still exist. According to the increase of electron density, bonding in $LiTi_2S_4$ is approximately an order of magnitude weaker than that in $LiTi_2O_4$. This may explain the fact why $LiTi_2O_4$ forms stable cubic spinel structures (39, 45–47), while the sulfur analogue $LiTi_2S_4$ does not exist.

AVERAGE INTERCALATION VOLTAGE

The average voltage E can be calculated as the change of the Gibbs energy ΔG^T between products and reactants divided by the Faraday constant F,

$$E = -\Delta G^T/F, \quad [1]$$

$$\Delta G^T = \Delta U + p\cdot\Delta V - T\cdot\Delta S. \quad [2]$$

It was demonstrated by Deiss *et al.* (15, 20) and Ceder *et al.* (16, 17, 19) that acceptable AIV values are obtained when both the volume ($p\cdot\Delta V$) and the entropy ($T\cdot\Delta S$) components of ΔG^T are neglected. This means that the dominant part of ΔG for a chemical reaction between solids originates from the change in internal energy ΔU. The AIV values calculated for the topotactic intercalation of Li into cubic spinels TiS_2 and TiO_2 according to the solid state reaction,

$$\mathrm{Li(metal)} + \mathrm{Ti}X_2\mathrm{(spinel)} \leftarrow \mathrm{(charge)(discharge)} \rightarrow \mathrm{LiTi_2}X_4\mathrm{(spinel)}\ (X = \mathrm{S, O}),$$

are listed in Table 3 along with available experimental values. Figure 6 shows an example of experimental voltages measured on the TiS_2 electrode. During the discharge the composition of the electrode continuously changes from TiS_2 to $LiTi_2S_4$. The measured voltage is the highest in the fully charged state. During the filling of Li sublattice it is continuously lowered usually showing a plateau. When the Li sublattice is filled the voltage suddenly drops. In our calculation only two states are considered: fully charged electrode TiS_2 and fully discharged compound $LiTi_2S_4$. Our calculated AIV therefore represents an average value for variably composed series $Li_xTi_2O_4$ ($x = 0 \rightarrow 1$) and should be comparable to the position of the measured plateau. Figure 6 shows a good agreement of our calculated AIV, indicated with the horizontal line, with plateaus of recent measurements on TiS_2 electrodes. The agreement is good in spite of the fact that measurements are performed with CVD prepared thin films of TiS_2 and calculations are done for cubic spinel TiS_2. This supports our previous conclusion that the voltage of the solid material does not depend on the structure but on the oxidation state of the transition metal (20).

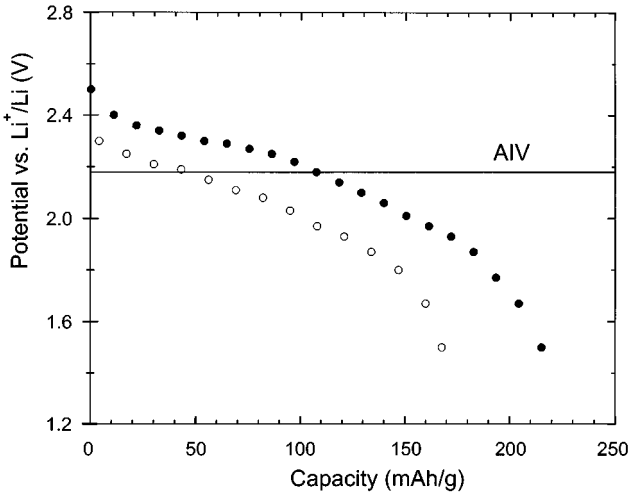

FIG. 6. The comparison of experimental discharge voltages of Li intercalated TiS_2 (25) and calculated average intercalation voltage.

For the purpose of comparison Table 3 also presents the AIV of cubic spinel $LiTi_2O_4$. The calculated voltage again is in good agreement with the values estimated from discharge and charge curves of the cubic $TiO_2/LiTi_2O_4$ (48). Note that the AIV strongly depends on the nonmetal atom and is much higher for oxides. To obtain more detailed information about factors which make the voltage of oxides higher we have calculated enthalpies of formation (EOF). Values presented in Table 3 show that the AIV is driven by the change of the EOF occurring between reactants and products during the intercalation. In the oxide structure the intercalated Li atoms are more stabilized compared to sulfide, what gives rise to the higher AIV for oxides.

TABLE 3
Enthalpies of Formation of $LiTi_2S_4$ and $LiTi_2O_4$ and Corresponding Li Deintercalated Cubic Spinel Structures (kJ/mol)[a] and Calculated Average Intercalation Voltage (V)

	TiS_2	$LiTi_2S_4$	TiO_2	$LiTi_2O_4$
EOF	3106.7	3611.5	4175.2	4754.8
ΔEOF	504.7		579.6	
AIV	2.16		2.93	
AIV (exp.)	2.0–2.3[b]		2.6–3.0[c]	

[a]ΔEOF of Li(metal/atomic) is 296.7 kJ/mol.
[b]Estimated from Ref. (25).
[c]Estimated from Ref. (48).

ACKNOWLEDGMENTS

This work is supported by Swis Federal Office of Energy. We thank Ľ. Smrčok for assistance with retrieving structural data, P. Blaha for numerous discussions on the computer code WIE97, and G. Che for providing us with experimental data on voltages of discharge experiments of TiS_2 electrode. Comments of one anonymous reviewer helped us to improve this work considerably.

REFERENCES

1. K. Brandt, *Solid State Ionics* **69,** 173 (1994).
2. "Lithium Batteries" (G. Pistoia, Ed.), Industrial Chemistry Library, Vol. 5. Elsevier, Amsterdam, 1994.
3. K. Sawai, Y. Iwakoshi, and T. Ohzuku, *Solid State Ionics* **69,** 273 (1994).
4. T. Iijima, K. Suzuki, and Y. Matsuda, *Synth. Met*, **73,** 9 (1995).
5. R. Koksbang, J. Barker, H. Shi, and M. Y. Saidi, *Solid State Ionics* **84,** 1 (1996).
6. T. Nagaura, M. Nagamine, I. Tanabe, and N. Miyamoto, *Prog. Batt. Solar Cells* **8,** 84 (1989).
7. T. Nagaura and K. Tozawa, *Prog. Batt. Solar Cells* **9,** 209 (1990).
8. K. Ozawa, *Solid State Ionics* **69,** 212 (1994).
9. M. Broussely, F. Perton, P. Biensan, J. M. Bodet, J. Labat, A. Lecerf, C. Delmas, A. Rougier, and J. P. Pérès, *J. Power Sources* **54,** 109 (1995).
10. F. K. Shokoohi, J. M. Tarascon, and D. Guyomard, *Prog. Batt. Batt. Mater.* **14,** 199 (1996).
11. F. Bonino, L. Busani, M. Lazzari, M. Manstretta, B. Rivolta, and B. Scrosati, *J. Power Sources* **6,** 261 (1981).
12. G. Pistoia, L. Li, and G. Wang, *Electrochim. Acta* **37,** 63 (1992).
13. J. N. Reimers, *J. Power Sources* **54,** 16 (1995).
14. K. Miura, A. Yamada, and M. Tanaka, *Electrochim. Acta* **41,** 249 (1996).
15. E. Deiss, A. Wokaun, J.-L. Barras, C. Daul, and P. Dufek, *J. Electrochem. Soc.* **144,** 3877 (1997).
16. G. Ceder, M. K. Aydinol, and A. F. Kohan, *Comput. Mater. Sci.* **8,** 161 (1997).
17. M. K. Aydinol, A. F. Kohan, and G. Ceder, *J. Power Sources* **68,** 664 (1997).
18. T. Zheng and J. R. Dahn, *Phys. Rev. B* **56,** 3800 (1997).
19. M. K. Aydinol, A. F. Kohan, G. Ceder, K. Cho, and J. Joannopoulos, *Phys. Rev. B* **56,** 1354 (1997).
20. L. Benco, J.-L. Barras, M. Atanasov, C. Daul, and E. Deiss, *Solid State Ionics* **112,** 255 (1998).
21. L. Benco, J.-L. Barras, C. Daul, and E. Deiss, *Inorg. Chem.* **38,** 20 (1999).
22. C. Wolverton and A. Zunger, *J. Electrochem. Soc.* **145,** 2424 (1998).
23. C. Wolverton and A. Zunger, *Phys. Rev. Lett.* **81,** 606 (1998).
24. M. S. Whittingham, *Prog. Solid State Chem.* **12,** 41 (1978).
25. G. Che, K. B. Jirage, E. R. Fisher, and C. R. Martin, *J. Electrochem. Soc.* **144,** 4296 (1997).
26. C. Umrigar, D. E. Ellis, D.-S. Wang, H. Krakauer, and M. Posternak, *Phys. Rev. B* **26,** 4935 (1982).
27. I. Oftedal, *Z. Phys. Chem.* (*Leipzig*) **134,** 301 (1928).
28. P. Ganal, P. Moreau, G. Ouvrard, M. Sidorov, M. McKelevy, and W. Glaunsinger, *Chem. Mater.* **7,** 1132 (1995).
29. P. Lightfoot, F. Krok, J. L. Nowinski, and P. G. Bruce, *J. Mater. Chem.* **2,** 139 (1992).
30. S. N. Patel and A. A. Balchin, *Z. Kristallogr.* **164,** 273 (1983).
31. J. R. Dahn, W. R. McKinnon, R. R. Haering, W. J. L. Buyers, and B. M. Powell, *Canad. J. Phys.* **58,** 207 (1980).
32. H. Hallak and P. Lee, *Solid State Commun.* **47,** 303 (1983).
33. H. Hallak and P. Lee, *Z. Kristallogr.* **164,** 273 (1983).
34. D. Singh, "Plane waves, pseudopotentials and the LAPW method." Kluwer Academic, Amsterdam, 1994.
35. P. Blaha, K. Schwarz, and J. Luitz, WIEN97. Vienna University of Technology, Vienna, 1997.
36. J. P. Descalaux, *Comp. Phys. Commun.* **216,** 1 (1969).
37. D. D. Koelling and B. N. Harmon, *J. Phys. C.*: *Solid State Phys.* **10,** 3107 (1977).
38. J. P. Perdew and Y. Wang, *Phys. Rev. B* **45,** 13244 (1992).
39. J. A. Campa, M. Velez, C. Cascales, E. Gutierez-Puebla, and M. A. Monge, *J. Cryst. Growth* **142,** 87 (1994).
40. Ľ, Benco, *Solid State Commun.* **94,** 861 (1995).
41. Ľ. Benco, *Ceram. Int.* **24,** 333 (1998).
42. P. Dudešek, Ľ. Benco, C. Daul, and K. Schwarz, *J. Phys. C*: *Condens. Matter* **10,** 1 (1998).
43. R. Hoffmann, "Solids and Surfaces: A Chemist's View of Bonding in Extended Structures." VCH Publishers, New York, 1988.
44. Ľ. Benco, *J. Solid State Chem.* **128,** 121 (1997).
45. A. Deschancres, B. Raveau, and Z. Sekkal, *Mater. Res. Bull.* **6,** 699 (1971).
46. J. R. Cava, D. W. Murphy, and S. J. Zahurak, *J. Solid State Chem.* **53,** 64 (1984).
47. J. Akimoto, Y. Gotoh, K. Kawaguchi, and Y. Oosawa, *J. Solid. State Chem.* **96,** 446 (1992).
48. K. M. Colbow, J. R. Dahn, and R. R. Haering, *J. Power Sources* **26,** 397 (1989).